ISSN: 2476-6909; Modares. Mech. Eng. *;*(*):*-*

Modares Mechanical Engineering

DOI:
journal homepage: mme.modares.ac.ir

Analysis of Hydrogen Distribution Near the Crack Tip via the Crystal Plasticity Framework

Majid Hemmatzadeh[1*], Iradj Sattari-Far[1], Mohammad Silani[2]

[1] Department of Mechanical Engineering, Amirkabir University of Technology, Tehran, Iran
[2] Department of Mechanical Engineering, Isfahan University of Technology, Isfahan, Iran

In Press, Pre-Proof Version

ARTICLE INFO

Article Type
Original Research

Article History
Received: **** **, *
Revised: **** **, *
Accepted: *** **, *
ePublished: **** **, *

ABSTRACT

Hydrogen embrittlement in steels causes changes in mechanical behavior under static and fatigue loads. The most important and fundamental topic in studying hydrogen embrittlement is the analysis of hydrogen diffusion in the steel structure. In this work, a micromechanical model based on coupled crystal plasticity and hydrogen diffusion is developed and applied to model hydrogen diffusion and storage in ferrite- pearlite microstructure of A516 Gr.70 steel. Particular emphasis is laid on mechanical influences on hydrogen transport, invoked by internal stresses and by trapping of dislocations generated by plastic strains. Crystal orientations measured by electron backscatter diffraction (EBSD) were mapped onto precise scanning electron microscopy (SEM) micrographs of ferrite and pearlite morphologies. Crystal plasticity model was carried out using the representative volume element (RVE) generated from the EBSD analysis. The homogenized stress–strain curve of the realistic RVE was validated with the experimental data. Based on the ferrite-pearlite structure of the material and the results of EBSD analysis, the developed finite element model was used to investigate the effect of the crack tip location on hydrogen distribution after mechanical loading and using a fracture initiation parameter (FIP), the likelihood of failure at different points was examined. It was determined that the hydrogen concentration and FIP in the pearlite phase are higher than in the ferrite phase; however, the dimensions under maximum hydrogen concentration are larger in the ferrite phase.

Keywords: Hydrogen embrittlement; Ferrite-pearlite microstructure; EBSD; Crystal plasticity model; Fracture initiation parameter

How to cite this article
M. Hemmatzadeh, I. Sattari-Far, M. Silani, Analysis of Hydrogen Distribution Near the Crack Tip via the Crystal Plasticity Framework. Modares Mechanical Engineering; *(*): ****-****.

*Corresponding author's email: majidh69@aut.ac.ir
*Corresponding ORCID ID: 0000-0001-7031-0010

Copyright© 2026, TMU Press. This open-access article is published under the terms of the Creative Commons Attribution-NonCommercial 4.0 International License which permits Share (copy and redistribute the material in any medium or format) and Adapt (remix, transform, and build upon the material) under the Attribution-NonCommercial terms.

شاپا: ۲۴۷۶-۶۹۰۹؛ مهندسی مکانیک مدرس. *؛*(*):* _*
مهندسی مکانیک مدرس
DOI:
صفحه اصلی مجله:mme.modares.ac.ir

بررسی توزیع هیدروژن در ناحیه نوک ترک با استفاده از پلاستیسیته بلوری

مجید همت زاده[*۱]، ایرج ستاری فر[۱]، محمد سیلانی[۲]

[۱] گروه مهندسی مکانیک، دانشگاه صنعتی امیرکبیر، تهران، ایران
[۲] گروه مهندسی مکانیک، دانشگاه صنعتی اصفهان، اصفهان، ایران

اطلاعات مقاله

نوع مقاله
مقاله پژوهشی

تاریخچه مقاله
دریافت: **/**/****
بازنگری: **/**/****
پذیرش: **/**/****
ارائه آنلاین: **/**/****

چکیده

تردی هیدروژنی می تواند باعث تغییر در خواص مکانیکی فولادها تحت تاثیر بارگزاری استاتیکی و خستگی شود. مهم ترین موضوع در بررسی پدیده تردی هیدروژنی، تحلیل نفوذ هیدروژن در ساختار فولاد می باشد. در این مطالعه یک مدل میکرو مکانیکی با استفاده از مدل سازی هم زمان پلاستیسیته بلوری و نفوذ هیدروژن جهت تحلیل نفوذ و توزیع هیدروژن در ریز ساختار فریت پرلیتی فولاد A516 Gr.70 تحت بارگزاری استاتیکی ارائه می شود. در این مدل با در نظر گرفتن تنش‌های داخلی و کرنش پلاستیک که باعث به دام افتادن هیدروژن در نابه جایی ها می شوند، اثر بارگزاری مکانیکی بر نفوذ هیدروژن تحلیل می شود. جهت مدل سازی دقیق ریز ساختار فولاد مذکور با استفاده از تصویر برداری الکترونی (SEM) و پراش الکترونی (EBSD)، دانه بندی و جهات کریستالی فریت و پرلیت موجود در ریز ساختار اندازه گیری و مشخص گردید. حجمک نماینده (RVE) مورد استفاده در مدل پلاستیسیته بلوری با توجه به نتایج آنالیزهای EBSD و SEM ایجاد و با اعمال بار گزاری مکانیکی و مقایسه نتایج تنش و کرنش با مقادیر حاصل از آزمون کشش پارامترهای موادی پلاستیسیته بلوری محاسبه و اعتبار سنجی گردید. با استفاده از مدل المان محدود بیان شده اثر محل قرارگیری نوک ترک در نقاط مختلف ریز ساختار بر توزیع هیدروژن و پارامتر جوانه زنی ترک بررسی می شود. مشخص گردید مقدار هیدروژن و پارامتر جوانه زنی ترک زمانی که نوک ترک در فاز پرلیت قرار دارد بیشترین مقدار را دارند و زمانی که نوک ترک در فاز فریت قرار گیرد این مقادیر کاهش می یابند و احتمال وقوع شکست زمانی که نوک ترک در فاز پرلیت قرار دارد بیشتر می باشد.

کلیدواژه‌ها: تردی هیدروژنی، میکرو ساختار فریت- پرلیت، مدل پلاستیسیته بلوری، پارامتر جوانه زنی ترک

نحوه ارجاع به این مقاله
همت زاده مجید، ستاری فر ایرج، سیلانی محمد، بررسی توزیع هیدروژن در ناحیه نوک ترک با استفاده از پلاستیسیته بلوری، مهندسی مکانیک مدرس. * (*): ****-****.

*پست الکترونیکی نویسنده عهده‌دار مکاتبات: majidh69@modares.ac.ir
*شناسه ارکید نویسنده عهده‌دار مکاتبات: ۰۰۰۰-۰۰۰۱-۷۰۳۱-۰۰۱۰

Copyright© 2026, TMU Press. This open-access article is published under the terms of the Creative Commons Attribution-NonCommercial 4.0 International License which permits Share (copy and redistribute the material in any medium or format) and Adapt (remix, transform, and build upon the material) under the Attribution-NonCommercial terms.

Press, Pre-Proof Version

1- Introduction

The penetration of hydrogen into metals significantly alters their mechanical properties, particularly when these materials operate in hydrogen-rich environments. This change is typically characterized by reduced ductility and increased brittleness effects collectively known as hydrogen embrittlement. Various mechanisms, including increased local plasticity and the deterioration of atomic bonding, contribute to the vulnerability of certain steels to hydrogen embrittlement [1].

Hydrogen is the smallest atom that can effortlessly penetrate metals and cause brittleness even in trivia quantities [2]. Hence, determining the distribution of hydrogen in metals is pivotal in investigating hydrogen embrittlement. Hydrogen diffusion in metals occurs through the atomic lattice or due to dislocations and trapping sites. As such, factors such as temperature, pressure, strain, and stress emanating from mechanical loading markedly affect hydrogen concentration [3]. Foster et al. were amongst the early researchers proposing the theory of dissolved hydrogen mobility in trapping site-containing iron lattices [4], where they employed source-sink terms to solve their proposed equation of diffusion. Next, the work of Foster et al. was redeveloped by Oriani [5] by assuming local equilibriums between trapped and mobile populations concerning restrained trap coverage degree domains. Entrenched in Oriani's theory, McMeeking et al. [6] proposed the hydrogen transport equation associated with the marked deformative plastic-elastic behavior of materials. They captured the effects of hydrostatic stress and the density of trapping sites, which intensifies along with the plastic deformation of the material. The model of hydrogen transport delivered in [6] was proved by Krom et al. [7] to fail in affording a precise hydrogen balance. Thus, Krom et al. modified the formerly coined hydrogen diffusion model by defining a strain rate (SR)-dependent factor that declines hydrogen concentrations in lattice sites upon trap site filling. Eventually, Gobbi [8] and Barrera [9] modeled hydrogen diffusion in metals by reflecting all the influential factors (i.e., trapping sites, strain, and stress emanating from mechanical loading) and validated the model with analytical and experimental results. The present research works with Gobbi's model [8] to simulate hydrogen diffusion and crystal plasticity (CP) equations.

Research has broadly studied the hydrogen diffusion coupled with CP to quantify hydrogen concentrations in metals under mechanical loading. For instance, Hassan et al. [10] used a micromechanical model encompassing hydrogen diffusion and coupled CP to quantify hydrogen concentrations in an RVE generated from ferrite crystals. Kaidi Li et al. [11] used a hybrid hydrogen diffusion/non-local CP constitutive model reflecting characteristics of grain boundary (GB) and incorporating fracture initiation for single crystal and polycrystalline nickel. Kumar et al. [12] merged CP (based on dislocation density) and hydrogen transport (based on the slip rate) models for simulating hydrogen-triggered deforming crack-tip damages for single bcc crystal with unique orientation. Elsewhere, Arnaudov et al. [13] studied fatigue life computational modeling reflecting hydrogen diffusions in metal microstructures for ferritic stainless steels.

In all the mentioned studies, the material consists of only one type of crystal, such as ferrite crystal. However, the steel used in the present study has a ferrite-pearlite structure, and the distribution of hydrogen in crystals with different structures is studied. Moreover, in studies examining hydrogen embrittlement, the localization of hydrogen at the crack tip plays a crucial role. This study examines how the crack tip's position within the crystal structure influences hydrogen distribution after mechanical loading, employing a hydrogen diffusion model integrated with crystal plasticity. Also, using a fracture initiation parameter (FIP), the likelihood of failure at different points is examined. SEM and EBSD results have been used to create RVE in all stages of the research. Accurately defining material parameters for crystal plasticity models is crucial. Ideally, these parameters can be derived from tensile tests conducted on fabricated single-crystal specimens with varying crystallographic orientations [14,15]. Calibrating material parameters for the crystal plasticity finite element model of A516 Gr. 70 steel presents significant challenges due to its ferrite-pearlite structure. This study conducts the calibration by comparing measured true stress versus true inelastic strain responses of A516 Gr. 70 steel. This research covers material characterization in Section II and proposes CP and hydrogen diffusion models in Section III. Section III covers crack tip modeling and describes geometric models and the boundary conditions intended for simulations. The results are discussed in Section IV, and the research concludes in Section V.

Table 1 Alloying composition of A516 Gr. 70 steel.

Fe	C	Si	Mn	P	Cr	Ni
Base	0.15	0.26	1.13	0.02	0.0634	0.033

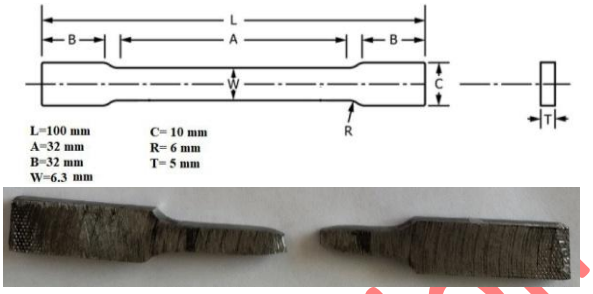


Fig. 1 Dimensions of the specimen used for the tensile test [24].

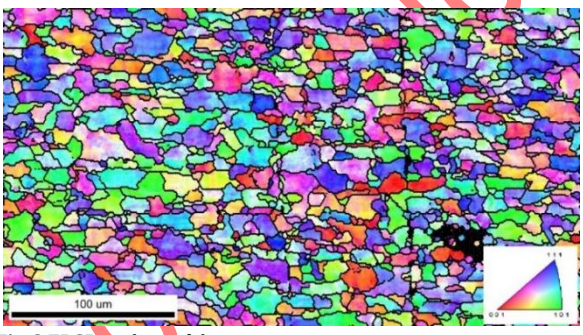


Fig. 2 EBSD analysis of the microstructure.

2-Material characterization

This study focuses on A516 Gr. 70 steel, characterized by its ferrite-pearlite microstructure. The average composition of its chemical composition is presented in Table 1.

Regarding the mechanical properties of A516 Gr. 70 steel as determined from the stress-strain curve, the specimens are extracted following the standard "ASTM E8-11" [16], with the specific dimensions of the specimen illustrated in Fig.1.

The numerical methodology entails the intended area's crystallographic orientation and morphology to be precisely represented for use as inputs for numerical simulations. As such, it is pivotal to specify how pearlite colonies and ferrite grains are arranged and in what way all the ferrite grains and matrix are crystallographically oriented in the pearlite colonies. Hence, the material's polished surfaces cut out is crucial to be investigated to characterize the orientation and grain morphology of ferrite grains. Likewise, an EBSD detector-equipped SEM imaging system is required to scan an area of roughly 350 × 150 μm^2. Fig. 2 illustrates the EBSD orientation map using pole figure color coding. Fig. 3 shows the results of EBSD and SEM with a smaller scale. In the SEM image, the white areas show the pearlite structure and the dark areas have the ferrite structure.

3-Modeling framework

The modeling framework consists of three integrated modules: CP formulation, the hydrogen diffusion formulation, and crack tip description. The crack tip model is embedded within the coupled diffusion-deformation calculations.

3-1-CP formulation

The CP theory is used to elucidate the crystal's mechanical behavior, with the relevant equations briefly stated in the following. Fig. 4

In Press, Pre-Proof

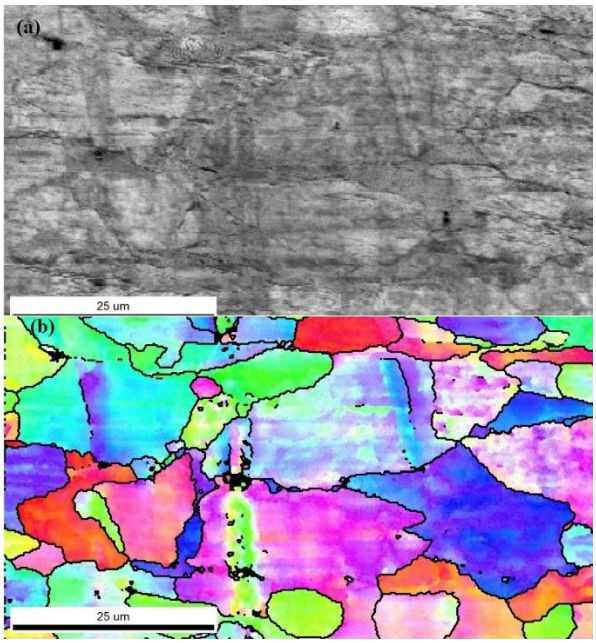


Fig. 3 Microstructure analysis of the A516 Gr.70 ferrite pearlite steel microstructure. SEM image is shown in **(a)** and EBSD characterization of the grain morphology is illustrated in **(b)**.

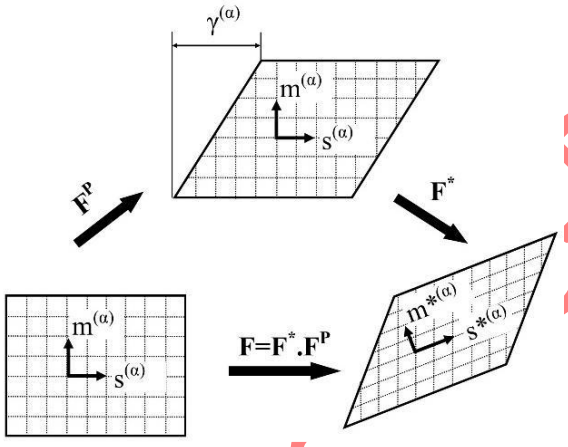


Fig. 4 Schematic representation of crystal deformation [17].

schematically shows the deformation mechanism for the single crystal, including plastic and atomic lattice deformations. The plastic deformation is only due to dislocation movement along slip systems, where this phenomenon does not structurally impact the crystal's lattice parameters and crystalline orientations. Next, the crystal lattice experiences rigid body rotations and stretching [17].

The F value (denoting overall deformation gradient) is given as follows [18]:

$$F = F^{*}.F^{P} \tag{1}$$

where the gradient of lattice (F^{*}) and plastic (F^{P}) deformations are specified. The primary slip system (α) is characterized by a vector $S^{(\alpha)}$ aligned with the slip direction and a vector $m^{(\alpha)}$ perpendicular to the slip plane.

As illustrated in Fig. 4, while the length and orientation of these vectors remain unchanged throughout plastic deformation, the lattice deformation alters their direction and magnitude. After changing the shape and direction of the vectors, the corresponding equations are as follows [18]:

$$S^{*(\alpha)} = F^{*}.S^{(\alpha)} \tag{2}$$

$$m^{*(\alpha)} = m^{(\alpha)}.F^{*\,-1} \tag{3}$$

Due to lattice stretching, the vectors $m^{*(\alpha)}$ and $S^{*(\alpha)}$ are generally non-unit but remain orthogonal. The plastic deformation gradient is expressed as [19]:

$$F^{P}.\dot{F}^{P} = \sum_{\alpha=1}^{n} \dot{\gamma}^{\alpha}\left(S^{(\alpha)} \otimes m^{(\alpha)}\right) \tag{4}$$

Where the shear strain (SS) γ^{α} on the slip system α is given; likewise, n denotes the counts of the crystal's active slip systems. As such, the current or deformed velocity gradient (L) is given as follows:

$$L = \dot{F}\,.F^{-1} = D + \Omega \tag{5}$$

For each variable, hereafter, the upper dot sign implies the time-relevant derivative. The velocity gradient further splits into the components Ω (asymmetric; denoting continuum spin rate) and D (symmetric; denoting deformation rate), which can be decomposed into plastic and lattice parts as follows:

$$L^{*} = D^{*} + \Omega^{*} = \dot{F}^{*}\,.F^{*\,-1} \tag{6}$$

$$L^{P} = D^{P} + \Omega^{P} = \sum_{\alpha=1}^{n} \dot{\gamma}^{\alpha}\left(s^{*(\alpha)} \otimes m^{*(\alpha)}\right) \tag{7}$$

The theory proposed by Hill and Rice [20] specifies that the single crystal's elastic properties are robust against dislocation slipping, with the governing law formulated below:

$$\overset{\nabla}{\tau}* = \Gamma : D^{*} \tag{8}$$

Where Γ denotes a 4-order symmetric tensor involving the crystal's elastic parameters, and $\overset{\nabla}{\tau}*$ denotes the rotating frame, Kirchoff stress Jaumann rate with the lattice (Ω^{*}):

$$\overset{\nabla}{\tau}* = \dot{\tau} - \Omega^{*}\sigma + \sigma\Omega^{*} \tag{9}$$

Where $\dot{\tau}$ refers to the Kirchoff stress material derivative. The $\overset{\nabla}{\tau}*$ value (for rotating frames with material (Ω)) is obtained as follows:

$$\overset{\nabla}{\tau} = \dot{\tau} - \Omega\sigma + \sigma\Omega \tag{10}$$

As with Schmid's law [21] and along τ^{α} (the slip direction), the shear stress resolved on the slip plane (if rising to a critical value $(\tau^{\alpha}{}_{cr})$ triggers plastic yielding or slip system slipping. As with Pan and Rice [22], SS rates on slip systems are a function of Schmid stress current value, which is quantified using the power law below:

$$\dot{\gamma}^{\alpha} = \dot{\gamma}_{0}\left[\frac{\tau^{\alpha}}{g^{\alpha}}\right]^{\frac{1}{n}} \tag{11}$$

Where $\dot{\gamma}_{0}$ denotes the reference SS rate, the exponent $1/n$ specifies the crystal's sensitivity to the plastic SR, and g^{α} describes the α slip system's current strength. For each state, $(\tau^{\alpha}{}_{cr})$ takes a critical value obtained from g^{α}. Variations in gα value (specified by the equation below) signify the crystal's strain strain-hardening (SSH) properties:

$$\dot{g}^{\alpha} = \sum_{\beta=1}^{n} h_{\alpha\beta}\,|\dot{\gamma}|^{(\beta)} \tag{12}$$

Where $h_{\alpha\beta}$ (as a function of γ) denotes the SH moduli. Peirce et al. [23] defined the crystal's SSH moduli using the equation below:

$$h_{\alpha\beta} = qh(\gamma) + (1-q)\,h(\gamma)\delta_{\alpha\beta} \tag{13}$$

Where q takes a constant value, $\delta_{\alpha\beta}$ denotes the Kronecker function, and $h(\gamma)$ is calculated from the equation below:

$$h(\gamma) = h_{0}\sec h^{2}\left|\frac{h_{0}\gamma}{\tau_{s} - \tau_{0}}\right| \tag{14}$$

Where initial values for hardening moduli (h_{0}) and yield stress (τ_{0}) are given. Likewise, τ_{s} denotes the saturated flow stress, and γ is the current overall SS, covering all slip systems:

$$\gamma = \sum_{\alpha=1}^{n} \gamma^{\alpha} \tag{15}$$

In Press, Proof Version

3-2-Hydrogen diffusion formulation

Hydrogen infiltrates metal matrixes readily and then accumulates in exact areas. Theoretically, the C value (overall hydrogen concentration) covers both C_L (hydrogen dispersed in metal lattice) and C_T (trapped hydrogen). The C_T side contains hydrogen confined in the metal's porous structures and defects. As such, the relevant equation for each metal's exact interior location is as follows [9]:

$$C = C_L + C_T \tag{16}$$

$$C_L = \beta \theta_L N_L \tag{17}$$

Where β is the count of hydrogen trapped sites accessible per the material's each atom. The θ_L value (0 to 1) denotes the portion of hydrogen-filled empty atomic lattice sites. Thus:

$$N_L = \frac{\rho N_A}{A_r} \tag{18}$$

This equation implies the overall count of atoms per the material's unit volume, where ρ is the material's density, N_A denotes the Avogadro value, and A_r is the material's atomic weight. C_T (denoting hydrogen concentrations trapped in defects) is obtained as follows:

$$C_T = \alpha \theta_T N_T \tag{19}$$

Where α is the count of hydrogen trapping sites and N_T is the overall count of probable atomic positions in defected sites. Upon a surge in plastic deformations, the N_T value surges gradually. The θ_T value (0 to 1) specifies the volume of hydrogen-filled defected sites. For the ρ_d value (defect density), N_T is obtained as follows:

$$N_T(\varepsilon p) = \sqrt{2}\frac{\rho_d(\varepsilon p)}{a} \tag{20}$$

Where a is the lattice constant value. hydrogen is quantified using moles per volume (M/V) as the preferential unit:

$$\bar{C_L} = \frac{C_L}{N_A} \tag{21}$$

$$\bar{C_T} = \frac{C_T}{N_A} \tag{22}$$

Research [28, 29] has defined equations adopted for hydrogen models. A brief overview of the key equations is provided here. The formulation below contains hydrogen mass flux vector [27]:

$$J_m = \frac{D_L V_H \bar{C_L}}{RT}\nabla\sigma_P - D_L \nabla \bar{C_L} \tag{23}$$

Where D_L defines hydrogen diffusion rates (at room temperature) within lattice interstices. The steel's microstructural properties temperature-dependently affect the D_L value. V_H (hydrogen partial molar volume) takes a constant value of 2×10-^{6} m^3/mol, [24], σ_P is the material's interior pressure stress, and $\nabla\sigma_P$ is the pressure stress spatial gradient.

Hydrogen flux inside the material is correlated to variations in hydrogen concentration via the parameter "mass balance". In the absence of internal hydrogen sources, changes in total hydrogen concentration (Ω) must balance the hydrogen flux across the peripheral surface S, resulting in:

$$\frac{\partial}{\partial t}\int_\Omega (\overline{C_T} + \overline{C_L})\, d\Omega + \int_S J.n\, dS = 0 \tag{24}$$

The outward normal vector (n) corresponding to (S) is defined. Eq. (24) contains two unknowns $\overline{C_T}$and $\overline{C_L}$. Based on Oriani [5], "lattice" and "trapped" hydrogen concentrations are assumed to be equal. Such equilibrium links both variables of concentration, allowing for $\overline{C_T}$ once $\overline{C_L}$ to be quantified. Combining relations (19) and (22) results in:

$$\overline{C_T} = \frac{N_T\theta_T}{N_A} = \frac{N_T}{N_A}\frac{1}{1+\frac{1-\theta_T}{\theta_T}} \tag{25}$$

$$\frac{\theta_T}{1-\theta_T} = K\theta_L \tag{26}$$

where K represents the equilibrium constant, dependent on the trap binding energy (W_B).

$$K = \exp\left(\frac{-W_B}{RT}\right) = const \tag{27}$$

For the hydrogen transport model, the ultimate formulation that covers how the diffusion process is impacted by mechanical deformation (based on McMeeking et al. [6]) and the plastic SR term proposed by Krom et al. [7] is as follows:

$$\frac{\partial \overline{C_L}}{\partial t}\left(1+\frac{\partial \overline{C_T}}{\partial \overline{C_L}}\right) + \nabla.\left(\frac{D_L V_H \overline{C_L}}{RT}\nabla\sigma_H\right) - \nabla.(D_L\nabla\overline{C_L}) + \frac{\partial \overline{C_T}}{\partial \overline{N_T}}\frac{d\overline{N_T}}{d\varepsilon_P}\frac{d\varepsilon_P}{dt} = 0 \tag{28}$$

hydrogen diffusion was simulated in Abaqus FEA by making an analogy between heat transfer and hydrogen diffusion equations (Table 2 in [9]). Concerning material behavior, UMATHT and UMAT subroutines were used to precisely integrate these equations. For all simulations, plane strain quadrilateral elements (having 4 integration points (CPE8RT) and 8 nodes) were intended for modeling the coupled hydrogen and CP.

Table 2 The correlation between heat transfer and hydrogen diffusion principles [9].

Heat transfer equations	Hydrogen diffusion equations
$\rho C_p\frac{\partial T}{\partial t} + \nabla.J_q + r_q = 0$	$\frac{C_T}{\partial t} + \nabla.J_m + r_m = 0$
Rate of change of thermal energy per unit mass $U_q = \frac{\partial C_T}{\partial t}$	Derivative of total hydrogen concentration $\frac{\partial C}{\partial t} = \frac{\partial (C_L + C_T)}{\partial t}$
Heat transfer flux: J_q	Hydrogen diffusion flux: $J = -\frac{D_L V_H \bar{C_L}}{RT}\nabla\sigma_H - D_L\nabla\bar{C_L}$
Heat source: r_q (Assume r_q=0)	Hydrogen source r_m (Assume r_m=0)
Density: ρ	1 unity

Table 3 Hydrogen diffusion coefficient [25,26].

Phase	Diffusion coefficient (m^2/s)
ferrite	$6 * 10^{-11}$ [25]
pearlite	$5 * 10^{-9}$ [26]

In the stated equations, the hydrogen diffusion coefficient D_L is dependent on temperature, considering that the analysis of the present study is performed at ambient temperature and also A516 Gr.70 steel includes ferrite-pearlite structure, the hydrogen diffusion coefficient is assumed to be constant according to Table 3.

3-3-RVE generation and homogenization scheme for driving macroscopic quantities

The RVE dimensions will have a significant impact on the results obtained from the crystal plasticity model. The RVE must be sufficiently large to capture the material's behavior accurately while remaining small enough to minimize computation time. A RVE with dimensions of 100 x 100 μm^2 and mesh configuration according to the EBSD analysis data presented in section 2 is developed. RVE grain morphology and mesh configuration according to EBSD data are shown in Fig. 5, the RVE contain 12078 CPE8RT elements.

In Press, Pre-Proof Version

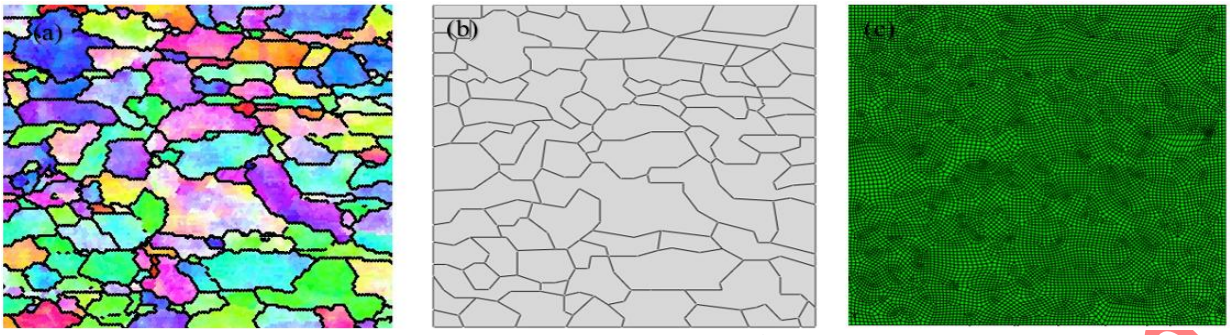


Fig. 5 (a) RVE grain morphology according to EBSD data, **(b)** grain boundaries, **(c)** mesh configuration.

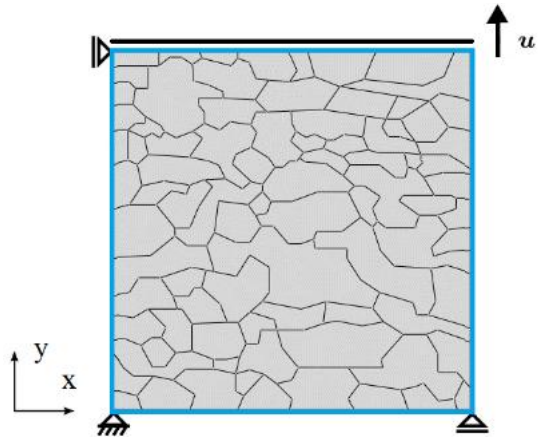


Fig. 6 RVE boundary condition.

Considering that the purpose of creating the mentioned model is to calculate the macroscopic characteristics of the material (e.g., the S-S curve), the modeling of metallurgical defects is neglected in this research. Thus, a homogenization scheme calculates the metal's macroscopic mechanical behavior using CP simulations and microstructural data.

As illustrated in Fig. 6, the RVE is y-directionally pulled by loading (under controlled displacement) to reach the yield point. The RVE's lower edge is fully y-directionally restricted ($U_y = 0$), while the RVE's two upper-left and lower-left nodes are fully x-directionally restricted ($U_x = 0$) to hamper rigid body motions.

The volume averaging method [27] is a reliable technique to derive macroscopic values from RVE simulations. This technique allows for calculating strain components and macroscopic stress using the equations below:

$$\langle\sigma\rangle_{ij} = \sum_{m=1}^{n_g} f_m^g \langle\sigma_m^g\rangle_{ij} \quad (29)$$

$$\langle\varepsilon\rangle_{ij} = \sum_{m=1}^{n_g} f_m^g \quad (30)$$

Where for the grain m, $f_m^g = \frac{V_m^g}{V^{RVE}}$ denotes the volume fraction (i.e., the RVE's volume/total volume ratio), and n_g denotes the count of RVE grains. For stress and strain (in the grain m), $\langle\sigma_m^g\rangle_{ij}$ and $\langle\varepsilon_m^g\rangle_{ij}$ are the ij-th components, which are obtained from the equations below:

$$\langle\sigma_m^g\rangle_{ij} = \sum_{q=1}^{n_{ip}} f_q^{ip} \langle\sigma_q^{ip}\rangle_{ij} \quad (31)$$

$$\langle\varepsilon_m^g\rangle_{ij} = \sum_{q=1}^{n_{ip}} f_q^{ip} \langle\varepsilon_q^{ip}\rangle_{ij} \quad (32)$$

In Eq. (32), n_{ip}denotes the overall count of integration points (for m), and f_q^{ip}represents the volume fraction for q (the integration point).

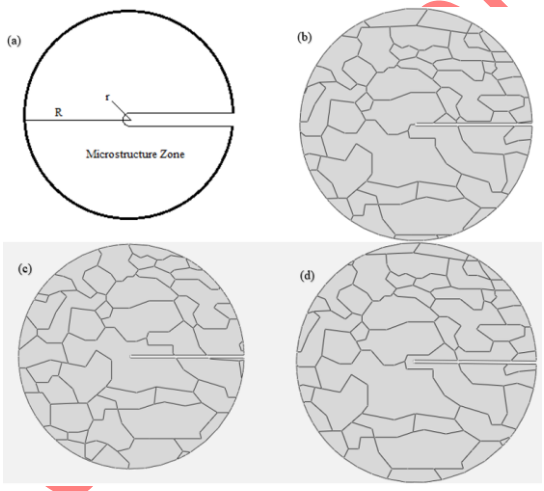


Fig. 7 (a) Crack domain , **(b)** crack tip positioned at grain boundary, **(c)** crack tip positioned at pearlite grain, **(d)** crack tip positioned at ferrite grain.

3-4-Crack tip description

Under plane strain conditions, the boundary layer method reflects hydrogen diffusion concentration [28]. A notch-containing circular domain is modeled as shown in Fig. 7(a). For the blunting crack, initial opening (r) and outer (R) radii are r = 0.5μm and R=4mm. On the outer boundary, this research merely reflects K_I (as the first term) and defines Mode I boundary terms as displacements, u_x and u_y, while cantering the polar coordinates system at the crack tip. Poisson's ratio (ν) and Young's modulus (E) are given. The stress intensity factor (K_I) takes the value of 25MPa$\sqrt{(m)}$ in this research. In the model, an initial concentration of $C_0^{initial}$ =7ppm (7×10-^{13}mol/mm^3) hydrogen is set to all nodes, as the highest amount of hydrogen in A516 gr.70 steel is 7ppm [29]. The hydrogen concentration on boundaries is kept constant C_0 =7ppm, with the boundary condition governing node displacements on the circular boundary u_x and u_y [28]:

$$u_x(r,\theta) = \frac{K_I}{E}\sqrt{\frac{r}{2\pi}}\,(1+\nu)cos\,(\frac{\theta}{2})(3-4\nu-cos\theta) \quad (33)$$

$$u_y(r,\theta) = \frac{K_I}{E}\sqrt{\frac{r}{2\pi}}\,(1+\nu)sin\,(\frac{\theta}{2})(3-4\nu-cos\theta) \quad (34)$$

This research reflects how hydrogen diffusion at crack tips is affected by microstructural morphology. Using the EBSD data from Fig. 5(a), the crack tip was located at three different points. After applying the same loading, the hydrogen distribution was investigated in each model. Three locations were considered: the grain boundary, pearlite grain, and ferrite grain, as shown in Figs. 7 (b, c, and d), respectively.

3-5-Fracture initiation parameter (FIP)

This section examines hydrogen distribution near the crack tip after applying mechanical loading. Before discussing the results, it is better to investigate the effect of hydrogen distribution on hydrogen

In Press, Pre-Proof

Table 4 Ferrite crystal plasticity parameters [32] and calculated pearlite crystal plasticity parameters.

CP Parameter	Symbol	Ferrite	Pearlite	unit
Reference slip rate	γ_0	0.001	0.001	1/s
Initial slip resistance	τ_0	100	63	MPa
Saturation slip resistance	τ_∞	225	154	MPa
Initial hardening modulus	h_0	500	800	MPa
Slip rate sensitivity	m	50	50	-
Hardening exponent	a	1	1	-

embrittlement phenomena, especially crack initiation and crack growth. In studies conducted regarding hydrogen embrittlement, the presence of a precise criterion for crack initiation is of great importance. Eq. (35), proposed by Kumar [12], is used as a proper criterion for predicting crack initiation in the presence of hydrogen in recent studies [11,12]. *FIP* is the fracture initiation parameter, and at the point where FIP is highest, crack initiation occurs.

$$FIP = \gamma_{acc}^{P}[1 + \frac{\sigma_{HS}}{\sigma_{eq}} + \frac{C_{Tot}}{C_{crit}} + \frac{\sigma_{HS}}{\sigma_{eq}}\frac{C_{Tot}}{C_{crit}}] + \frac{\sigma_{HS}}{\sigma_{eq}}\frac{C_{Tot}}{C_{crit}} \quad (35)$$

Where γ_{acc}^{P} is accumulated plastic slip in the microstructure, $\sigma_{eq}$and σ_{HS} are the equivalent and hydrostatic stress respectively, C_{crit} is the threshold hydrogen concentration at or above which macroscopic hydrogen embrittlement has been experimentally observed to occur and C_{Tot} is hydrogen concentration. $C_{crit,}$ a is a constant parameter that is calculated using experimental methods, and its value is considered to be 3400 appm in this study [30]. Other parameters can be calculated easily in different points by the proposed model in this study.

4-Result and discussion

4-1-Crystal plasticity parameters

A516 Gr.70 steel has a ferrite-pearlite structure. In addition to determining the orientation of the crystals, it is necessary to determine their structure. The determination of ferrite or pearlite crystal structure and their orientation was done according to the results of EBSD and SEM analysis. The ferrite structure has a bcc lattice and 48 slip systems. Franciosi et al. [31] showed that the most important slip systems in this structure are the <110> system with 12 slip systems. Therefore, in this research, only the <110> slip system is modeled, which reduces the calculations. The elastic coefficients of ferrite and pearlite phases are considered to be the same as the elastic coefficients of A516 Gr.70 steel, with a Poisson's ratio of 0.3 and a Young's modulus of 207 GPa. Berisha et al. [32] calculated the ferrite crystal plasticity parameters at ambient temperature using experimental methods. In the present study, these results were used as the plastic properties of ferrite crystals according to table 4.

Pickering [33] presented the Eq. (36) to predict the yield stress of ferrite and pearlite phases in ferrite-pearlite steels:

By applying periodic boundary conditions and tensile loading on the volume indicated in Fig. 5, the pearlite crystal plasticity parameters are selected such that the experimental stress-strain curve and simulated outcomes are in the highest agreement with each other. The pearlite crystal plasticity parameters are reported in table 4.

Fig. 8 experimentally compares the stress-strain curve with the simulated results. As demonstrated, the stress-strain curve obtained from virtual experimentation on the RVE closely aligns with the experimental data.

4-2-Hydrogen distribution near crack tip

Fig. 9 shows the pressure stress and hydrogen distribution at the crack tip region after loading. The crack tips located at the grain boundary, the pearlite phase and the ferrite phase. The lowest pressure stress at the crack tip is in the pearlite phase, while the highest is in the ferrite

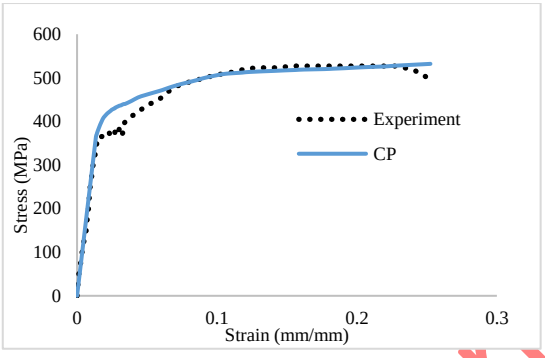


Fig. 8 Experimental and CP simulated stress-strain curve.

phase. According to Eq. (23), after applying mechanical loading, hydrogen is expected to move from regions with higher pressure stress to regions with lower pressure stress. As shown in Fig. 9(C) and 9(E), the highest hydrogen concentration is in the pearlite phase and the lowest in the ferrite phase. It should be noted that the region affected by the lowest pressure stress and the highest hydrogen concentration in the pearlite phase is significantly smaller than the ferrite phase. Additionally, the pressure stress and hydrogen distribution at the crack tip in the pearlite and ferrite phases is nearly symmetrical, whereas for the crack tip located on the grain boundary, it is not symmetrical. Also, the lowest pressure stress and the highest hydrogen concentration in the grain boundary region are in the pearlite phase.

Based on Eq. (25), the distribution of trapped hydrogen in dislocations can be calculated. The amount of trapped hydrogen is compared with the total hydrogen at the crack tip in Fig. 10. The distribution of trapped hydrogen accounts for approximately 16 percent of the total hydrogen. Additionally, the amount of hydrogen in the pearlite phase is higher. It is worth noting that the maximum hydrogen content in the pearlite phase occurs exactly at the crack tip, whereas for the ferrite phase and grain boundary, it occurs at a distance of about 1μm from crack tip.

Fig. 11 shows the value and distribution of the FIP parameter. As mentioned in Section 3.5, increasing the value of this parameter increases the likelihood of failure. The highest FIP parameter value is 2.67 at the crack tip region located in the pearlite phase, and the lowest value is 1.99 at the crack tip region located in the ferrite phase. However, the area affected by the highest FIP value in the ferrite phase is considerably larger than in the pearlite phase. Also, according to Fig. 11 (a), the FIP parameter value for the crack tip region located at the grain boundary is 2.12, and its distribution is such that the maximum value of this parameter is in the pearlite phase. Considering the points presented, it can be stated that the highest probability of failure occurs, in order, at the pearlite phase, the grain boundary, and the ferrite phase.

In Press, Pre-Proof Version

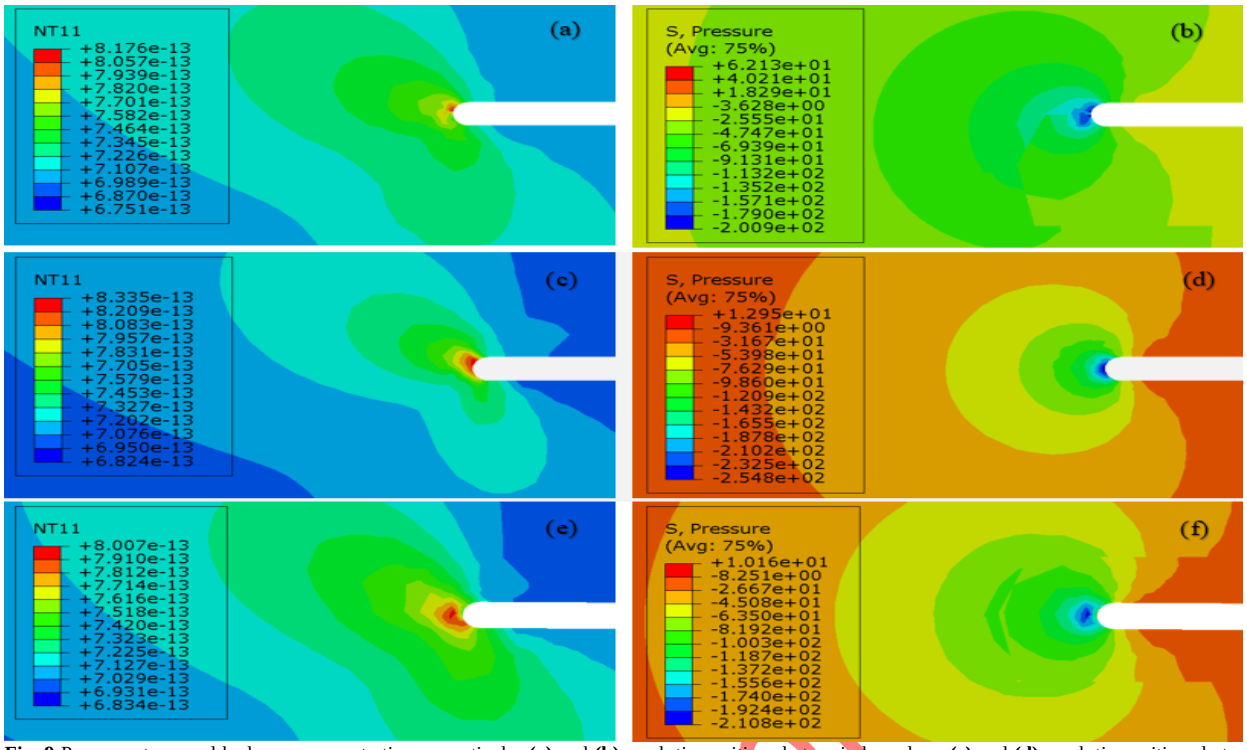


Fig. 9 Pressure stress and hydrogen concentration respectively: **(a)** and **(b)** crack tip positioned at grain boundary, **(c)** and **(d)** crack tip positioned at pearlite grain, **(e)** and **(f)** crack tip positioned at ferrite grain**.**

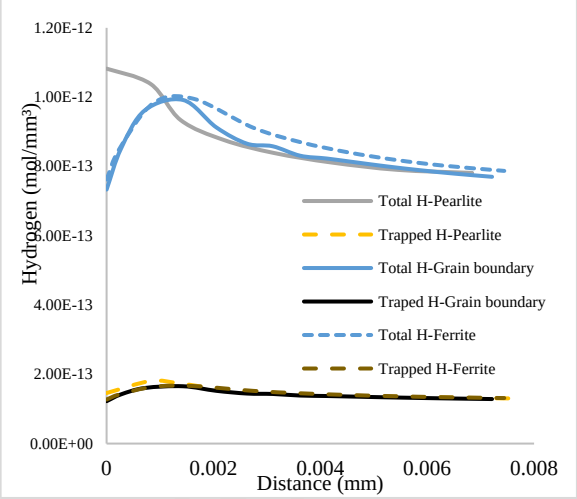


Fig. 10 Total and trapped hydrogen concentration at crack tip.

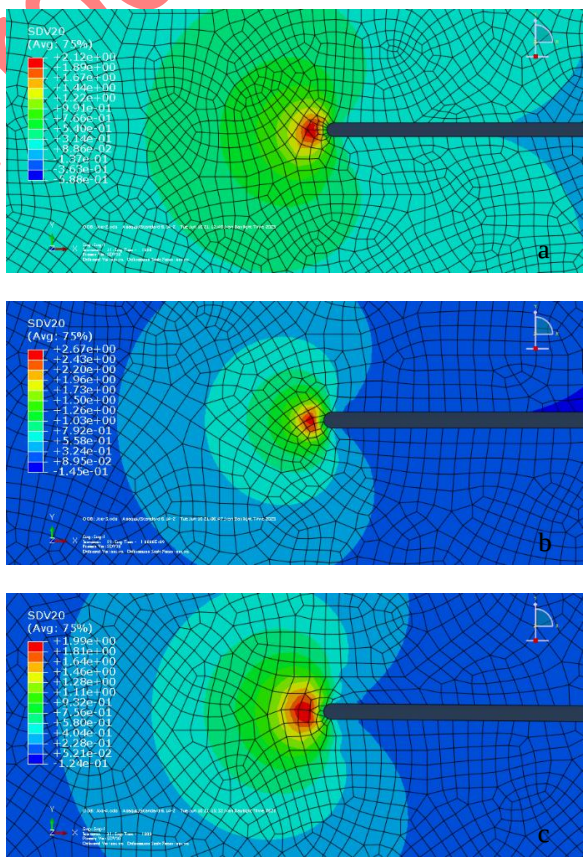


Fig. 11 FIP distribution respectively: **(a)** crack tip positioned at grain boundary, **(b)** crack tip positioned at pearlite grain, **(c)** crack tip positioned at ferrite grain.

5-Conclusions

This study presents a micromechanical model integrating CP and hydrogen diffusion to analyse hydrogen concentration, accounting for crack tip location and crystal phase influence. The examined steel in this research is A516 Gr.70 with a ferrite-pearlite microstructure, in which the initial crystal orientations are defined using EBSD and SEM methods. Consequently, the CP model was carried out using the RVE generated from the EBSD and SEM analysis.

Given the significant influence of crystal plasticity parameters on finite element model outcomes, these parameters are determined from tensile test results of hydrogen-free samples, based on appropriate assumptions, while disregarding the impact of hydrogen-induced variations. For this purpose, an RVE is first generated using EBSD and SEM analysis results. Then, boundary conditions and mechanical loading are applied, and the stress-strain curve is obtained using the volume averaging method and compared with the experimental tensile test. The ultimate parameters were calculated by iterating this step and modifying the crystal plasticity parameters. Noting that A516 Gr. 70 steel has a ferrite-pearlite structure, the finite element model was

In Press

employed to analyze the influence of crack tip location within pearlite and ferrite phases on hydrogen concentration following mechanical loading. The required circular domain in these analyses was generated with a radius of R = 4 mm and a crack with a radius of r = 0.5 μm according to EBSD analysis results. Ultimately, after applying mechanical loading, the hydrogen concentration, pressure stress and FIP were studied.

By locating the crack tip on the grain boundary, the largest hydrogen value was generated at the crack tip and in the pearlite phase, and the lowest pressure stress was observed in both the ferrite and pearlite phases, with the mentioned region in the ferrite phase having larger dimensions. For samples with the crack tip located in either the pearlite or ferrite phase, the hydrogen value in the pearlite phase are higher than in the ferrite phase; however, the dimensions under minimum pressure stress are larger in the ferrite phase. Judging based on FIP value, it can generally be stated that due to the generation of maximum values of FIP in the pearlite phase, the possibility of crack initiation is higher in this phase.

Ethics Approval :

The scientific content of this article is the result of the authors' research and has not been published in any Iranian or international journal.

Conflict of Interest:

This article includes some results from the corresponding author's doctoral dissertation. There are no other conflicts of interest to declare.

References

[1] M. Robertson, Hydrogen embrittlement understood, The Minerals, Metals & Materials Society and ASM International, 2015. doi: 10.1007/s11661-015-2836-1.

[2] A. Guillermo, Hydrogen embrittlement analysis in a CrMoV steel by means of sent specimens, heretical and Applied Fracture Mechanics, 2020. doi: 10.1016/j.tafmec.2019.102450.

[3] S. Dwivedi, Hydrogen embrittlement in different materials: A review. international journal of hydrogen energy, 2018, doi: 10.1016/j.ijhydene.2018.09.201.

[4] X. Cheng, H. Zhang, A new perspective on hydrogen diffusion and hydrogen embrittlement in low-alloy high strength steel, Corrosion Science, 2020. doi: 10.1016/j.corsci.2020.108800.

[5] R. Oriani, Diffusion and trapping of hydrogen in steel, Acta Metallurgical, 1970. doi: 10.1016/0001-6160(70)90078-7.

[6] P. Sofronis, R. McMeeking, Numerical analysis of hydrogen transport near a blunting crack tip, Journal of the Mechanics and Physics of Solids, 1989. doi: 10.1016/0022-5096(89)90002-1.

[7] A. Krom, R. Koers, A. Bakker, Hydrogen transport near a blunting crack tip, Journal of Mechanics and Physics of Solids, 1989. doi: 10.1016/S0022-5096(98)00064-7.

[8] G. Gobbi1, C. Colombo, A fully coupled implementation of hydrogen embrittlement in FE analysis, Advances in Engineering Software, 2019, doi: 10.1016/j.advengsoft.2019.04.004.

[9] O. Barrera, E. Tarleton, Modeling the coupling between hydrogen diffusion and the mechanical behaviour of metals, Computational Materials Science 122, 2016. doi: 10.1016/j.commatsci.2016.05.030.

[10] H. Hassan, A. Hartmaier, Micromechanical modeling of coupled crystal plasticity and hydrogen diffusion, Philosophical Magazine, 2018. doi: 10.1080/14786435.2018.1530466.

[11] Kaidi Li a, Bin Tang, Hydrogen diffusion behavior within microstructures near crack tip: A crystal plasticity study, Mechanics of Materials, 2024. doi: 10.1016/j.mechmat.2024.105032.

[12] R. Kumar, D. K. Mahajan, Modeling of hydrogen-assisted damage at the deforming single crystal crack-tip, Mechanics of Materials, 2023. doi: 10.1016/j.mechmat.2023.104557.

[13] N. Arnaudov, A. Kolyshkin, Micromechanical modeling of fatigue crack initiation in hydrogen Atmosphere, Mechanics of Materials, 2020. doi: 10.1016/j.mechmat.2020.103557.

[14] K. Sedighiani, M. Diehl, An efficient and robust approach to determine material parameters of crystal plasticity constitutive laws from macro-scale stress–strain curves, International Journal of Plasticity, 2020. doi: 10.1016/j.ijplas.2020.102779.

[15] Y. Miyazawa, F. Briffod, Prediction of Cyclic Stress–Strain Property of Steels by Crystal Plasticity Simulations and Machine Learning, Materials, 2019. doi: 10.3390/ma12223668.

[16] ASTM E8/E8M-11, Standard Test Methods for Tension Testing of Metallic Materials, doi:10.1520/E0008_E0008M-11.

[17] Yonggang Huang, A User-material subroutine incorporating single crystal plasticity in the ABAQUS finite element program, Division of Applied Sciences Harvard University Cambridge, Massachusetts, 1991.

[18] Lee EH. Elastic-plastic deformation at finite strains. 1969.

[19] Asaro RJ., Micromechanics of crystals and polycrystals, Advances in applied mechanics, 1983. doi: 10.1016/S0065-2156(08)70242-4.

[20] Hill R, Rice J. Constitutive analysis of elastic-plastic crystals at arbitrary strain, Journal of the Mechanics and Physics of Solids, 1972. doi: 10.1016/0022-5096(72)90017-8.

[21] Schmid E, Boas W. Plasticity of crystals. 1950.

[22] Pan J, Rice JR. Rate sensitivity of plastic flow and implications for yield-surface vertices, Journal of Solids and Structures, 1983. doi: 10.1016/0020-7683(83)90023-9.

[23] Peirce D, Asaro R, Needleman A. An analysis of nonuniform and localized deformation in ductile single crystals, Acta metallurgica, 1982. doi: 10.1016/0001-6160(82)90005-0.

[24] R. Oriani, The diffusion and trapping of hydrogen in steel, Acta Metallurgic 18, 1970. doi: 10.1016/0001-6160(70)90078-7.

[25] Vigdis O., Afaf S., FE simulation of hydrogen diffusion in duplex stainless steel, international journal of hydrogen energy, 2014. doi: 10.1016/j.ijhydene.2013.10.101

[26] Hideki hagi, Effect of interface between cementite and ferrite on diffusion of hydrogen in carbon steels, Material transections, JIM, 1994.

[27] Nemat-Nasser S. Averaging theorems in finite deformation plasticity, Mechanics of Materials, 1999. doi: 10.1016/S0167-6636(98)00073-8.

[28] Williams, M.L., On the stress distribution at the base of a stationary crack. Journal of Applied Mechanics, 1957. doi: 10.1115/1.4011454.

[29] M. Hemmatzadeh, I. sattari-far, M. silani, Experimental and Finite Element Study of A516 Steel Hydrogen Embrittlement, Metallurgical and Materials Transaction B, 2025. doi: 10.1007/s11663-024-03406-6.

[30] Arora, A., Kumar, R., Singh, H., Mahajan, D., 2021. Hydrogen assisted crack initiation in metals under monotonic loading: A new experimental approach. Theoretical and Applied Fracture Mechanics, 2021. doi: 10.1016/j.tafmec.2021.102917.

[31] P. Franciosi, L. T. Le, G. Monnet, C. Kahloun, Investigation of slip system activity in iron at room temperature by SEM and AFM in-situ tensile and compression tests of iron single crystals, International Journal of Plasticity, 2015. doi: 10.1016/j.ijplas.2014.09.008.

[32] Berisha, B., Raemy, C., Becker, C., Gorji, M., Hora, P., Multiscale modeling of failure initiation in a ferritic–pearlitic steel. Acta Material, 2015. doi: 10.1016/j.actamat.2015.08.035.

[33] F. B. Pickering, Physical Metallurgy and the Design of Steels, Applied Science Publisher , London, 1978.

In Press, Pre-Proof Version